



Full Length Article

Lithium storage kinetics of highly conductive F-doped SnO₂ interfacial layer on lithium manganese oxide surfaceDong-Yo Shin^a, Bon-Ryul Koo^b, Hyo-Jin Ahn^{a,b,*}^a Program of Materials Science & Engineering, Convergence Institute of Biomedical Engineering and Biomaterials, Seoul National University of Science and Technology, Seoul 01811, Republic of Korea^b Department of Materials Science and Engineering, Seoul National University of Science and Technology, Seoul 01811, Republic of Korea

ARTICLE INFO

Keywords:

Ultrafast lithium storage kinetics
F-doped SnO₂
Lithium manganese oxide
Cathode
Interfacial surface

ABSTRACT

Interfacial engineering of LiMn₂O₄ (LMO) is a promising candidate strategy to improve lithium storage performance of the cathode electrode in lithium-ion batteries (LIBs). However, although the use of interfacial engineering strategy showed a positive effect increasing cycling stability at the slow charge process due to the relaxed destruction of the LMO structure, there are unsatisfactory ultrafast lithium storage performances, which results from the extremely limited electrochemical kinetics. Therefore, in the present study, we newly developed a conductive F-doped SnO₂ (FTO) interfacial layer to implement superb lithium storage kinetics of LMO. As a result, there provide attractive functionalities in terms of efficient electron and Li⁺ diffusion, relaxed Mn dissolution and volume expansion at LMO, as well as an improved electrical conductivity at the electrode, resulting in the outstanding lithium storage performance (specific capacity of 76.6 mAh g⁻¹ with the capacity retention of 82.2% at 10 C), a superb cycling capability (the specific capacity of 114.9 mAh g⁻¹ and the capacity retention of 97.1% at 1 C), which is surpassing the results of previous studies. Therefore, this novel conductive FTO interfacial layer can be used as an effective route to improve ultrafast lithium storage kinetics of the LMO material in LIBs.

1. Introduction

In recent years, owing to the global issues of eco-friendliness and oil shortage over the world, much effort has been invested into replacing gasoline-powered devices by electrically-powered devices, such as electric vehicles and unmanned drones [1–3]. However, these devices still suffer from critical problems of low mileage and long charging time, which considerably limits their practical applications. Therefore, the diverse approaches, including the reduction of body weight, enhancement of motor efficiency, and improvement of battery performance, have become an important technology to improve the mileage and charging rate of the electrically-powered devices [4,5]. In particular, lithium-ion batteries (LIBs), due to their good cycling stability with high energy density, low memory effect, low self-discharge, and eco-friendliness, have become the main power source for the electric vehicles. However, the practical performances of the LIBs do not meet all the requirements, such as mileage over 300 miles and charging time above 10 min, to expand the demand of the electric vehicles [6,7]. Therefore, to overcome these problems, a challenging research to

obtain ultrafast lithium storage kinetics of the LIBs (named ultrafast LIBs) has been considered using the electrode materials (cathode and anode) [8,9]. Among the cathode materials of the LIBs, the spinal LiMn₂O₄ (LMO) is reported to be one of the potential materials for the LIBs due to its high theoretical capacity (148 mAh g⁻¹), high power density at high reaction voltage (3.5–4.5 V), non-toxicity, and cost-effectiveness [10–12]. Unfortunately, in the use of the LMO, the poor rate capability and cycling stability at ultrafast condition arises predominantly due to the following three main problems: (1) Mn dissolution and the Jahn-Teller distortion; (2) limited electron and Li⁺ diffusion rate; and (3) low electrical conductivity [13–15]. In order to improve the ultrafast lithium storage kinetics using the LMO, various approaches have been proposed through the LMO modification by surface coating, cation doping, and morphology control [16–19]. Among these new approaches, the surface coating by protecting layers (e.g., Al₂O₃, CeO₂, ZnO, and MoO₃) is a promising way to enhance lithium storage kinetics by suppressing the Mn dissolution and volume expansion or facilitating electron and Li⁺ diffusion of the LMO during charge/discharge processes [20–22]. However, although the reported

* Corresponding author at: Program of Materials Science & Engineering, Convergence Institute of Biomedical Engineering and Biomaterials, Seoul National University of Science and Technology, Seoul 01811, Republic of Korea.

E-mail address: hjahn@seoultech.ac.kr (H.-J. Ahn).

<https://doi.org/10.1016/j.apsusc.2019.144057>

Received 3 July 2019; Received in revised form 21 August 2019; Accepted 16 September 2019

Available online 01 October 2019

0169-4332/ © 2019 Elsevier B.V. All rights reserved.

surface coating demonstrated the improved lithium storage kinetics with cycling stability and rate capability at the low current density of 1–2 C, there was a rapid degradation of the lithium storage kinetics over 6 C due to the critical electrochemical behavior limiting the electron and Li^+ diffusion at the LMO electrode and generating a rapid destruction of the LMO structure, resulting in a poor ultrafast cycling stability with a low specific capacity. In this context, the development of a novel conductive interfacial layer with accelerated electrochemical kinetics is necessary to improve the ultrafast lithium storage kinetics for next-generation LIBs.

In the present study, we introduce a novel conductive interfacial layer of conductive F-doped SnO_2 (FTO) on the LMO surface for accelerating the electrochemical kinetics for the ultrafast LIBs. In particular, as F atoms substitute for O atoms in SnO_2 structure, FTO has a high electrical conductivity by formed extra electron as well as excellent physical/chemical stability by stable Sn-F bonds, which thus is chosen as interfacial layer to improve the lithium storage kinetics [23]. The FTO deposition is performed using the horizontal ultrasonic spray pyrolysis deposition (HUSPD), which is a solution-based process to form a uniform and dense thin-layer structure. This can be a competitive factor in our study due to the attractive advantages of the HUSPD characterized by cost-effectiveness and a simple system procedure as compared to the vacuum-based processes (e.g., magnetron sputtering, chemical vapor deposition, and atomic layer deposition). Introduction of the conductive FTO interfacial layer offers the advanced effects for the ultrafast lithium storage kinetics specifically, not only fastening the electron deliver rate at the electrode, but also improving electron and Li^+ diffusion and structural stability of the LMO. Therefore, the conductive FTO interfacial layer on the LMO surface displays an impressive ultrafast cycling capacity, as well as cycling stability and a high rate capability.

2. Experiments

2.1. Chemicals

Lithium manganese oxide (LiMn_2O_4 , LMO) powders were purchased from POSCO M-TECH. Tin (IV) chloride pentahydrate ($\text{SnCl}_4 \cdot 5\text{H}_2\text{O}$), ammonium fluoride (NH_4F), and ethyl alcohol ($\text{C}_2\text{H}_5\text{OH}$) were purchased from SAMCHUN, Sigma-Aldrich, and Duksan, respectively. All chemicals were used without further purification.

2.2. Introduction of conductive F-doped SnO_2 (FTO) interfacial layer on LMO surface

Conductive FTO interfacial layer on LMO surface was performed using horizontal ultrasonic spray pyrolysis deposition (HUSPD). For FTO deposition, the precursor solution was prepared by dissolving 0.68 M $\text{SnCl}_4 \cdot 5\text{H}_2\text{O}$ and 1.19 M NH_4F into mixed solvent with ethyl alcohol and deionized water, in which, the mole ratio of Sn/F was fixed at 1/1.76 to obtain the optimum performance of conductive FTO interfacial layer. And then, prepared solution was sprayed onto the LMO maintained at 420 °C in reaction chamber by an ultrasonic atomizer (1.6 MHz). During the HUSPD, the carrier gas flow rate and stage rotation speed were fixed at 15 L min^{-1} and 5 rpm. In order to optimize the ultrafast lithium storage kinetics of the LMO using the conducting FTO interfacial layer, the deposition time of the FTO was controlled to 0, 12, 20, and 28 min (herein designated as bare-LMO, FTO-LMO12, FTO-LMO20, and FTO-LMO28).

2.3. Characterization

The crystal structure was determined by X-ray diffraction (XRD) with $\text{Cu K}\alpha$ radiation in the 2 theta range from 10 to 90° with a step size of 0.02°. The chemical bonding states was investigated using X-ray photoelectron spectroscopy (XPS) with $\text{Al K}\alpha$ as X-ray source. The

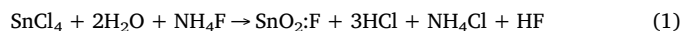
structure and morphology of all samples were analyzed using field-emission scanning electron microscopy (FESEM) and transmission electron microscopy (TEM). To examine the distribution of the elements in the FTO the LMO, the analysis of Energy-dispersive X-ray spectroscopy mapping (EDS-mapping) was performed. The electrical conductivity of all electrodes was examined using a Hall-effect measurement system (Ecopia, HMS-3000).

2.4. Electrochemical characterization

The electrochemical properties were analyzed using the coin-type cells (CR2032, Hohsen Corp.), which is composed of Li metal foil (Honjo Chemical, 99.8%) as an anode, the FTO-LMO samples as a cathode, a porous polypropylene membrane (Celgard 2400) as separator, and a 1.0 M LiPF_6 solution dissolved in mixture of dimethyl carbonate and ethylene carbonate (1:1) as electrolyte. The electrodes were prepared on an Al foil as current collector using the mixed slurry consisting of 70 wt% FTO-LMO samples as the active material, 10 wt% ketjen black as the conducting materials, and 20 wt% polyvinylidene fluoride as the binder in N-methyl-2-pyrrolidone. The electrodes were dried in a vacuum oven at 100 °C for 10 h. The mass loading amount of the FTO-LMO samples was optimized with $8.4 \pm 0.4 \text{ mg cm}^{-2}$. All the coin-type cells were assembled in an argon-filled glove box with maintained O_2 and H_2O contents below 5 ppm. Electrochemical impedance spectroscopy analysis was performed at frequency range of 10^2 kHz to 10^{-2} Hz by applying an AC signal of 5 mV. Charge-discharge tests of the electrodes were measured using a battery cycler system (WonATech Corp., WMPG 3000 model) in the potential range of 3.3–4.3 V (versus Li/Li^+). The cycling performance was demonstrated up to 100 cycles at current density of 1 C (128 mA g^{-1}). The rate performance was observed at current densities of 1C, 3C, 5C, 7C, and 10 C. The ultrafast lithium storage performance was examined up to 500 cycles at 10 C. The cyclic voltammetry curves were measured at a scan rate of 1 mV s^{-1} in the voltage of 3.3–4.3 V (versus Li/Li^+) by using a potentiostat/galvanostat (Ecochemie Autolab, PGST302N).

3. Results and discussion

Fig. 1 shows a schematic illustration of the HUSPD for formation of the conductive FTO interfacial layer on LMO surface. Owing to the horizontally supplied precursor solution by a uniform carrier gas flow into the reaction chamber, the HUSPD could produce a uniform layer structure of low thickness [23]. First, the droplets with F and Sn ions formed by ultrasonication were horizontally supplied onto the LMO surface by the carrier gas (see Fig. 1a). Second, the FTO was formed on the LMO surface by following the formation process (see Fig. 1b) composed of several steps, namely: (1) evaporation of the solvent; (2) condensation of the solute in droplets; (3) thermal decomposition. During thermal decomposition, the droplets wetted on the LMO surface could form the FTO interfacial layer by their heterogeneous nucleation (see the chemical reactions in Eq. (1)) [23].



Thereafter, the nucleated FTO interfacial layer was gradually stacked along the surface of the LMO, leading to the formation of the conformal and dense FTO thin layer on the LMO surface [24]. Therefore, the introduction of the novel conductive FTO interfacial layer on the LMO interfacial surface can act as both efficient charge diffusion and a stable protecting agent for the LMO to improve ultrafast LIB performance (see Fig. 1c).

Fig. 2a shows the XRD patterns of bare-LMO, FTO-LMO12, FTO-LMO20, and FTO-LMO28. The main characteristic diffraction peaks of all samples were found at 18.7°, 36.2°, 43.9°, and 63.9°, which corresponds to the (1 1 1), (3 1 1), (4 0 0), and (4 4 0) planes, respectively, of the LMO phase with the spinel structure (space group of Fd-3 m, JCPDS

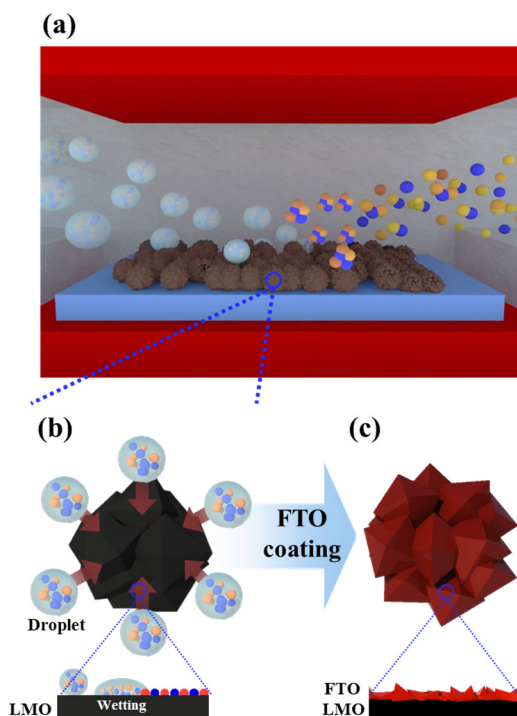


Fig. 1. Schematic illustration for formation mechanism of conductive FTO protecting layer on the LMO interfacial surface using the HUSPD.

card No. 035-0782) [25,26]. These results suggest that the LMO phase of all samples remains the spinel structure without any structural variation during the FTO deposition. In addition, due to the relatively small amount of the FTO as compared to the LMO, no diffraction peak related to the FTO phase is observed in the XRD results. However, with

an increase of the FTO deposition time, the diffraction peak intensities of (3 1 1) plane in FTO-LMO12, FTO-LMO20, FTO-LMO28 is decreased by 20%, 40%, and 57%, respectively, compared with the peak intensity of (3 1 1) plane in bare-LMO. In addition, as a result of Energy-dispersive X-ray spectrometry mapping (EDS-mapping), an atomic percent of F and Sn atoms of FTO-LMO were 0.59% and 11.95% for FTO-LMO12, 0.80% and 16.38% for FTO-LMO20, and 1.30% and 24.04% for FTO-LMO28, respectively. This result is in agreement with the XRD result (see Fig. S1). To confirm the chemical states of the FTO on the LMO, the XPS analysis was performed. The binding energies emitted from the XPS spectrum (see Fig. 2b–d) were calibrated using the binding energy of C 1s (284.5 eV) used as reference. Fig. 2b shows the full scan spectrum of FTO-LMO20 with F 1s, Mn 2p, O 1s, and Sn 3d peaks, indicating the presence of F, Mn, O, and Sn elements without another impurity phase. In Fig. 2c, the Sn 3d XPS spectrum of FTO-LMO20 shows two major peaks at 486.6 eV for Sn 3d_{5/2} and 495.1 eV for Sn 3d_{3/2}, indicating the existence of Sn⁴⁺ state related to SnO₂ phase [23,26]. In addition, a minor peak at 487.7 eV for Sn 3d_{5/2} and 496.3 eV for Sn 3d_{3/2} was emitted, which is consistent with the Sn-F state related to the formation of the FTO phase, as confirmed by F 1s spectra (see Fig. 2d) [23,26]. The effect of F doping into SnO₂ lattices can improve their electrical conductivity by creating extra free electrons [23]. Furthermore, the formed free electrons increased the electrical conductivity to achieve a faster charge transport at the entire electrode. In addition, as shown in Fig. S2, the Mn 2p XPS spectra of FTO-LMO20 had two different signals at 642.4 eV for Mn 2p_{3/2} and 654.1 eV for Mn 2p_{1/2}, with the energy separation of 11.7 eV and consisting of the Mn(IV) (red area) and Mn(III) (blue area) states with the 1:1 area ratio, suggesting the existence of the LMO phases with the 1:1 stoichiometric ratio of Mn(IV) and Mn(III) [11,27]. Therefore, the XRD and XPS results prove the presence of the FTO formed on LMO using the HUSPD.

Fig. 3 shows (a–d) low-magnification and (e–h) high-magnification FESEM images of bare-LMO, FTO-LMO12, FTO-LMO20, and FTO-

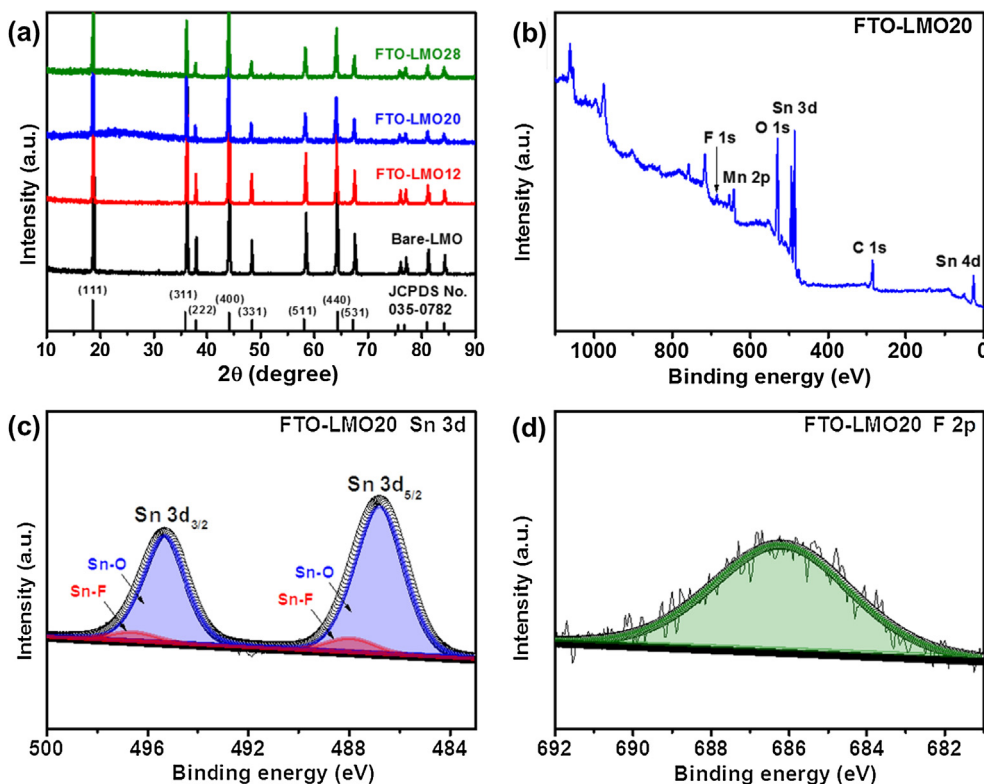


Fig. 2. (a) XRD patterns of bare-LMO, FTO-LMO12, FTO-LMO20, and FTO-LMO28, (b) XPS full scan spectrum of FTO-LMO20, and XPS spectra obtained from (c) Sn 3d (d) F 1s of FTO-LMO20.

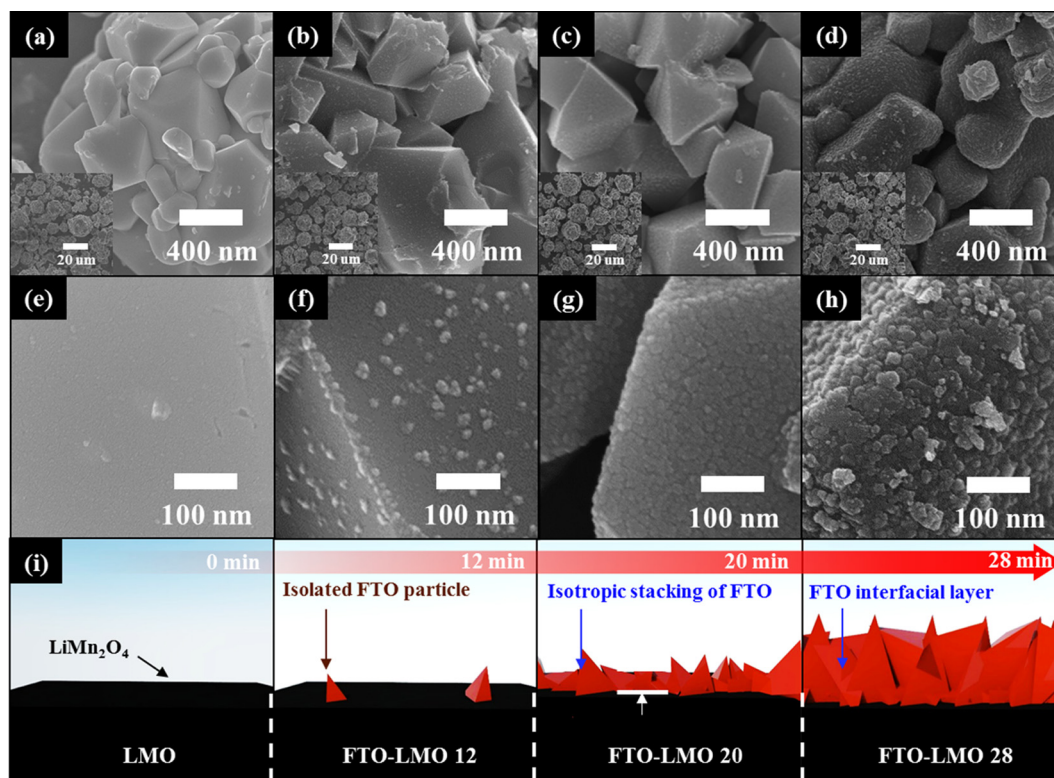


Fig. 3. (a–d) Low and (e–h) high-magnification FESEM images of bare-LMO, FTO-LMO12, FTO-LMO20, and FTO-LMO28 and (i) schematic illustration for formation of the conductive FTO protecting layer with thin-layer structure with the deposition time of the HUSPD.

LMO28, respectively. Bare-LMO shows the aggregated structure of 10.4–18.8 μm in diameter (see the insets of Fig. 3a) composed of primary particles with the diameter of 204.8–496.2 nm (see Fig. 3a). With an increase of the FTO deposition time, gradual enhancement of the diameter on the aggregators from 206.4 to 499.3 nm for FTO-LMO12 to 231.5–525.8 nm for FTO-LMO20 was observed (see Fig. 3b–d). This indicates that the FTO deposition on the LMO was successfully performed by the HUSPD. In addition, while bare-LMO reveals a smooth surface of the primary particles (see Fig. 3e), for FTO-LMO12, FTO-LMO20, and FTO-LMO28, the FTO particles were observed on the LMO surface (see Fig. 3f–h). This phenomenon is directly related to the mechanism of the HUSPD to form a conformal and dense thin-layer on the LMO surface (see in Fig. 3i) [23,24,28]. That is, when the deposition time of FTO was 12 min, the isolated particles on the surface could be formed by the evaporation-condensation route of the droplets. With an increase of the FTO deposition time, the isotropic stacking of the developed particles was gradually generated along the LMO surface, leading to the formation of the conductive FTO interfacial layers of different thickness and morphology on the LMO by the adjustment of the FTO deposition time. Therefore, the structures of the conductive FTO interfacial layers coated on the LMO can act as an important factor in terms of improving ultrafast lithium storage kinetics. To further investigate the structures of the conductive FTO interfacial layer on the LMO surface, the analysis of transmission electron microscopy (TEM, Gwangju Center, Korea Basic Science Institute) was performed (see Fig. 4). Compared to bare-LMO (Fig. 4a), an interfacial layer structure was found to be covered on the LMO surface of FTO-LMO12, FTO-LMO20, and FTO-LMO28 (see Fig. 4b–d). In particular, while a rough thin-layer structure was formed due to the isolated FTO particles, FTO-LMO20 and FTO-LMO28 clearly showed the conformal and dense thin-layer structure along the LMO surface, which can play a protecting role by restraining the Mn dissolution and volume expansion of the LMO structure so that to improve cycling stability [11,29]. In addition, in a selected-area electron diffraction (SAED) analysis, the diffraction

patterns of LMO and FTO are shown by ring patterns corresponding to the (1 1 1) and (3 1 1) plane for LMO and (1 1 0) plane for FTO, respectively. (see Fig. S3) [30,31]. This interfacial layer structure of the FTO is also confirmed by the energy-dispersive X-ray spectrometry (EDS) mapping results of FTO-LMO20 to show the distribution of the Sn, F, and O atoms on the LMO (see Fig. S4). For the thickness of the conductive FTO interfacial layer, due to the growth of the FTO particles by the increase of the FTO deposition time, FTO-LMO28 (34.6–39.5 nm) is higher than that of FTO-LMO20 (9.1–14.4 nm). The higher thickness of the FTO layer over 30–40 nm can act as a Li^+ diffusion resistance to reduce the ultrafast LIB performances [32,33]. In addition, the inter-layer spacing of 4.78 \AA corresponding to the (1 1 1) plane of the LMO and that of 2.42 \AA corresponding to the (2 0 0) plane of the FTO are clearly observed in Fig. 4e and f, respectively. Specifically, the inter-layer spacing of the FTO is a larger value as compared to that of SnO_2 (2.40 \AA), which is due to the substitution of smaller O^{2-} (ionic radius 1.32 \AA) by F^- with a larger ionic radius (1.33 \AA) in the SnO_2 [34,35]. That is, when F is doped into SnO_2 lattices, the Sn-O bonding state is transferred to the Sn-F bonding state to produce free electrons, thereby providing an improvement of the electrical conductivity to offer an efficient electron transfer at the electrode during the ultrafast cycling process [36]. Accordingly, the SEM and TEM results show a successful formation of the novel conductive FTO interfacial layer on the LMO surface, which can be useful in improvement of ultrafast lithium storage kinetics by providing an efficient charge transfer and a good structural stability of the LMO. To investigate the electrical behavior of the samples with different thickness values of the conductive FTO interfacial layer, the electrical conductivity of the electrodes assembled with bare-LMO, FTO-LMO12, FTO-LMO20, and FTO-LMO28 was measured using the Hall effect measurement. As shown in Fig. 5, with an increase of the FTO deposition time, the electrical conductivity improved from $4.24 \times 10^2 \text{ S cm}^{-1}$ for the bare-LMO electrode to $6.28 \times 10^2 \text{ S cm}^{-1}$ for the FTO-LMO28 electrode. Specifically, the FTO-LMO20 ($6.25 \times 10^2 \text{ S cm}^{-1}$) and FTO-LMO28 electrodes ($6.28 \times 10^2 \text{ S cm}^{-1}$)

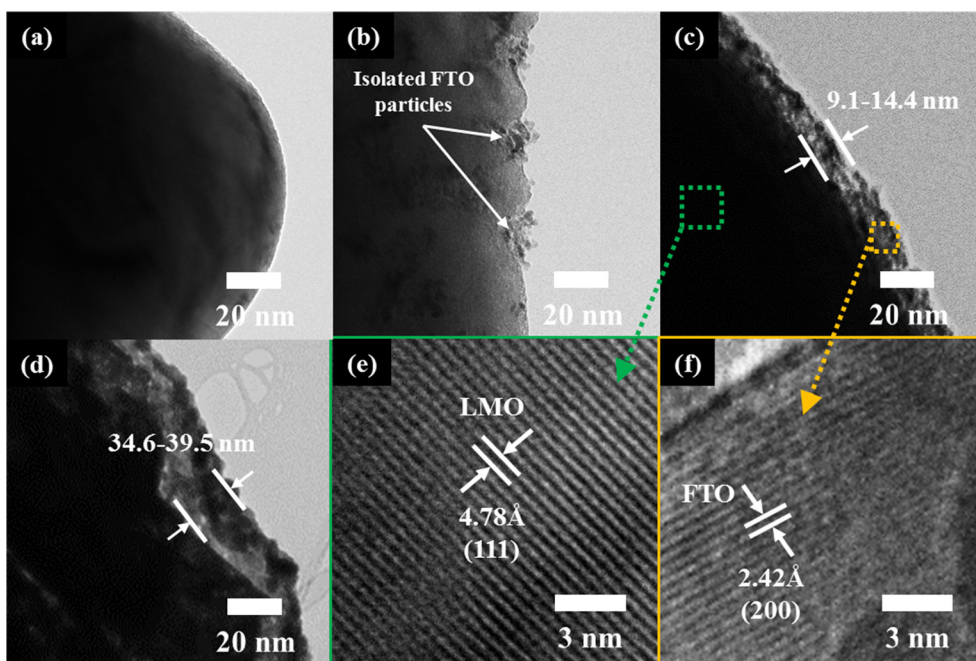


Fig. 4. (a–d) Low-magnification TEM images of bare-LMO, FTO-LMO12, FTO-LMO20, and FTO-LMO28, and (e–f) High-magnification TEM images obtained from the LMO and FTO of FTO-LMO20.

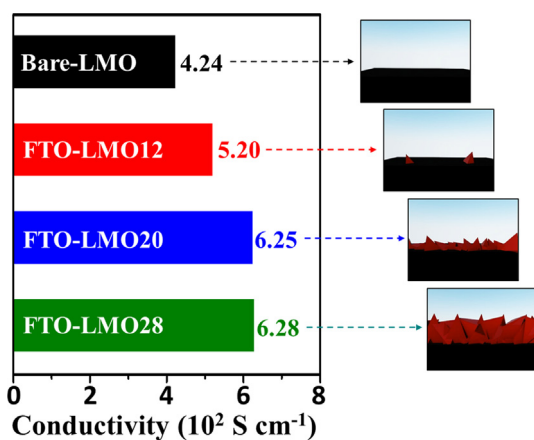


Fig. 5. Electrical conductivity of the electrodes fabricated from bare-LMO, FTO-LMO12, FTO-LMO20, and FTO-LMO28.

possess a higher electrical conductivity (1.47 times for the FTO-LMO20 electrode and 1.48 times for the FTO-LMO28 electrode) than the bare-LMO electrode. This led to an improvement of the electron transport rate at the electrode of the LIBs resulting from an increased thickness of the conductive FTO interfacial layer. Therefore, the conductive FTO interfacial layer can be helpful in terms of improving the ultrafast cycling performance by a fast electron transfer at the entire electrode. To investigate the electrochemical kinetics related to charge transfer resistance and Li^+ diffusion on the effect of the conductive FTO interfacial layer on the LMO, electrochemical impedance spectroscopy (EIS) analysis was performed using fresh cells constructed with bare-LMO, FTO-LMO12, FTO-LMO20, FTO-LMO28. Fig. 6a shows Nyquist plots of all cells at the open-circuit potential in the frequency range of 10^5 kHz to 10^{-2} Hz . The equivalent circuit used impedance analysis are in the insert of Fig. 6a. The semicircle in the high-frequency region and the inclined line in low-frequency region represent the charge transfer resistance (R_{ct}) at the electrode-electrolyte interface and Warburg impedance, respectively [37,38]. Due to the optimized thin thickness of the conductive FTO interfacial layer, the charge transfer resistance gradually reduced from bare-LMO to FTO-LMO20. However, FTO-LMO28 shows an increased charge transfer resistance compared to FTO-

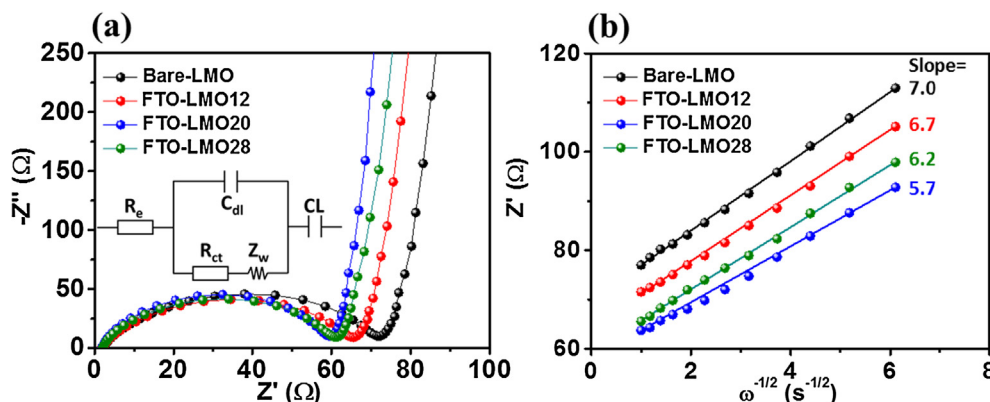


Fig. 6. (a) Nyquist plots and (b) relationship between Z''_{real} and $\omega^{-1/2}$ in the low frequency range of all electrodes.

LMO20, which can be attributed to the thick thickness to interfere Li^+ diffusion into the LMO. In addition, this behavior of the electrochemical kinetics is consistent with the result of Warburg impedance. As shown in Fig. 6b, Li^+ diffusion coefficient can be obtained from the low-frequency slope of Warburg impedance using Eqs. (2) and (3) [8,39].

$$Z_{\text{real}} = R_e + R_{\text{ct}} + \sigma_w \omega^{-1/2} \quad (2)$$

$$D = R^2 T^2 / 2 A^2 n^4 F^4 C^2 \sigma_w^2 \quad (3)$$

where R_e is bulk resistance of the cell, corresponding to the combined influence of electrode, electrolyte, and separator, σ_w is the Warburg impedance coefficient, D is the Li^+ diffusion coefficient, A is the electrode area, n is the number of electrons per molecule, R is the gas constant, F is the Faraday constant, and C is the molar concentration of Li^+ ions. The calculated Li^+ diffusion coefficient indicates that FTO-LMO20 has the highest value ($10.5 \times 10^{-12} \text{ cm}^2 \text{ s}^{-1}$) as compared to other samples ($6.9 \times 10^{-12} \text{ cm}^2 \text{ s}^{-1}$ for bare-LMO, $7.6 \times 10^{-12} \text{ cm}^2 \text{ s}^{-1}$ for FTO-LMO12, and $8.9 \times 10^{-12} \text{ cm}^2 \text{ s}^{-1}$ for FTO-LMO28 (see Fig. S5)). This observation suggests that the conductive FTO interfacial layer with the optimum thin thickness can efficiently enhance the ultrafast lithium storage performance of the LIBs by improving electrochemical kinetics of the LMO.

Fig. 7a shows the rate performance of all electrodes at the current density of 1 C, 3 C, 5 C, 7 C, and 10 C. With an increase of the current density, while the specific capacity of the bare-FTO electrode rapidly degraded, the electrodes coated with the FTO showed an increased specific capacity from FTO-LMO12 to FTO-LMO20. This is mainly induced to the facilitated electron and Li^+ diffusion on the LMO surface by the optimum thickness of the conductive FTO interfacial layer; however, for the FTO-LMO28 electrode, to thicker thickness of the conductive FTO interfacial layer, a decreased rate capability as compared to that of the FTO-LMO20 electrode is observed. In particular, specific capacity of FTO-LMO20 (88.6 mAh g^{-1}) at 10 C is higher than SnO_2 coated LMO (57.4 mAh g^{-1}) prepared by the same method as FTO-LMO20, which is due to higher electrical conductivity of FTO interfacial layer (6.25 S m^{-1}) compared to SnO_2 (4.33 S m^{-1}) (see Fig.

S6). In addition, in the initial charge-discharge stages, the specific capacity of all samples is gradually recovered due to activation of LMO which is required to store Li^+ ions into LMO structure. The rate capabilities at charge and discharge processes (see Fig. S7) of the FTO-LMO20 electrode demonstrate outstanding results as compared to previous reports of surface-coated LMO electrodes (see Fig. 7b) [22,40–49]. Specifically, as compared to the other electrodes, the FTO-LMO20 electrode shows a much better specific capacity of 114.9 mAh g^{-1} with the superb capacity retention of 97.1% after 100 cycles when cycled at the current density of 1 C, which is ascribed to the conformal and dense thin-layer structure of the conductive FTO interfacial layer that efficiently prevents the Mn dissolution and volume expansion of the LMO (see Fig. 7c). However, although the LIB performance using the LMO electrode is commonly remarkable at the general current density (1 C), the ultrafast cycling performance at 10 C for widening the application areas of the LIBs may rapidly decline due to the accelerated effect of critical destruction of the LMO structure by the Mn dissolution and volume expansion, as well as the limited electrochemical kinetics by the reduction of electron and Li^+ diffusion time [14,15]. In previous reports, although the protecting layers such as ZrO_2 and YF_3 were coated on the LMO, the rapid degradation of the ultrafast cycling capacity at 10 C as compared to 1 C was observed (75.0% for ZrO_2 and 45.5% for YF_3). Therefore, in the present study, in order to prove the effect of the conductive FTO interfacial layer on the LMO surface, we measured the ultrafast cycling performance of all electrodes at the current density of 10 C during 500 cycles. As shown in Fig. 7d, while the bare-LMO electrode displays an extremely low specific capacity of 31.6 mAh g^{-1} after 500 cycles with the capacity retention of 70.8%, there is a noticeable improvement of the ultrafast cycling performances with both a good specific capacity (76.6 mAh g^{-1}) and the capacity retention (82.2%) on the FTO-LMO20 electrode. These excellent performances can be mainly attributed to the introduction of the conductive FTO interfacial layer with the favorable electrical conductivity (see Fig. 5) that accelerates electron delivery at the electrodes during the ultrafast cycling process, as well as to the effects of the efficient charge transport (see Fig. 6) at the LMO and

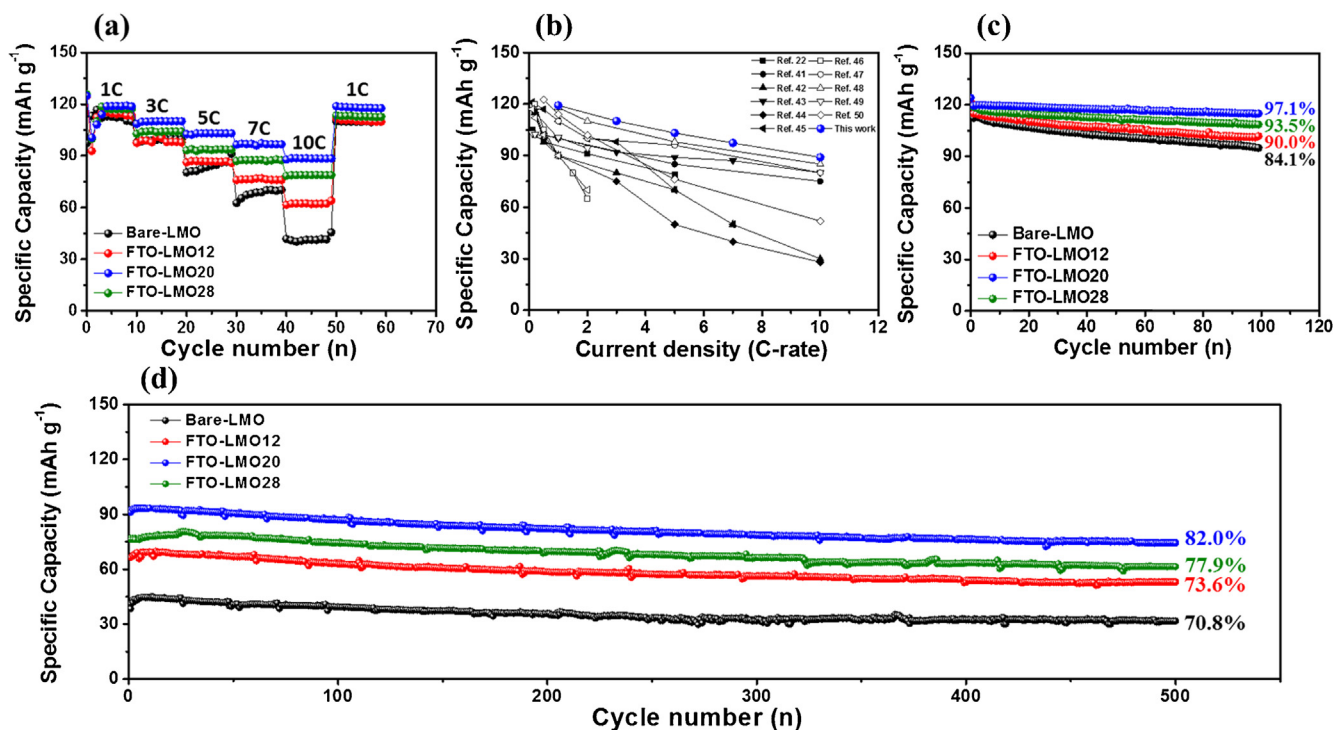


Fig. 7. (a) Rate-performance at current densities of 1 C, 3 C, 5 C, 7 C, 10 C, and 1 C, (b) Comparison of rate-performance with previously reported results of surface coated LMO cathode materials in the LIBs, (c) cycling stability at current density of 1 C up to 100 cycles, and (d) ultrafast cycling stability at 10 C up to 500 cycles.

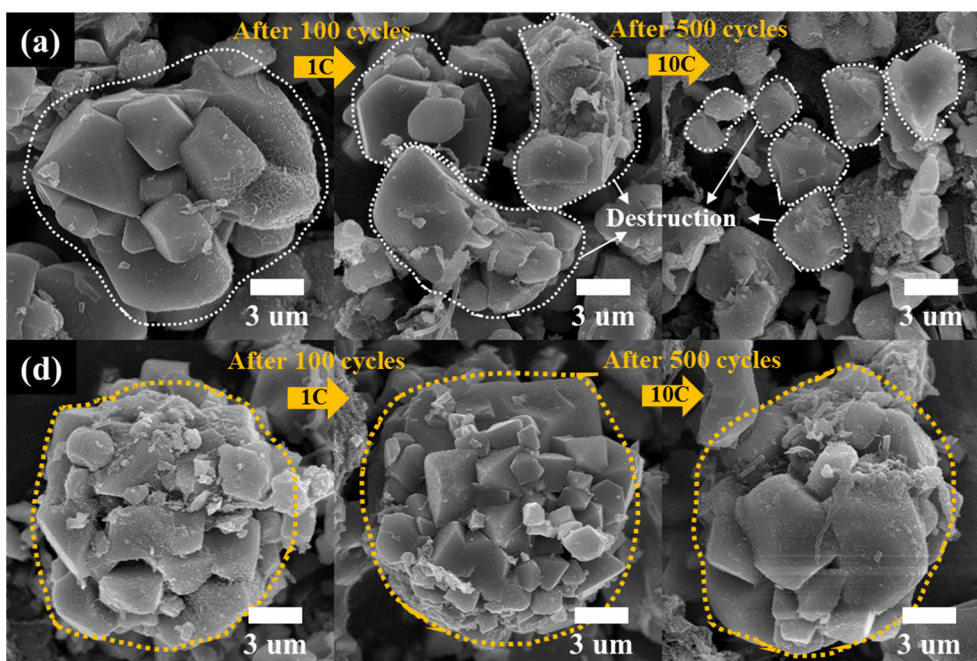


Fig. 8. FESEM images of (a) bare-LMO and (b) FTO-LMO20 after charging/discharging test at 1 C for 100 cycles and 10 C for 500 cycles.

structural prevention of the LMO (see Fig. S8). To trace the function of the conductive FTO interfacial layer on the structural stability of the LMO during the ultrafast cycling process, the comparison of the structure variation between the bare-LMO (Fig. 8a) and FTO-LMO20 electrode (Fig. 8b) obtained from decomposed coin-type cell was performed using the FESEM measurement. After 100 cycles at 1 C, while the bare-LMO electrode showed a partial destruction of the LMO structure, the FTO-LMO20 electrode completely maintained an aggregated structure without any structural variation. This is due to the relaxation of Mn dissolution resulting from Jahn-Teller distortion by the conductive FTO interfacial layer, which is proved by the reduced shift of anodic and cathodic peaks after 50 cycles at the scan rate of 1 mV s^{-1} on the FTO-LMO20 electrode ($\pm 0.017 \text{ V}$) as compared to that of the bare-LMO electrode ($\pm 0.039 \text{ V}$) (see CV curves of Fig. S9) [50,51]. In the CV curves, the first cathodic peak ($\sim 3.9 \text{ V}$) is exhibited by removed Li ions in tetrahedral sites having Li-Li interaction. The second cathodic peak ($\sim 4.1 \text{ V}$) is attributed to the removal of Li ions from the remaining tetrahedral sites in non-interaction site. Furthermore, at the ultrafast cycling process (current density of 10 C), the aggregated structure of the bare-LMO electrode was completely destroyed to form the isolated particles after 500 cycles. On the other hand, the FTO-LMO20 electrode clearly retained the primary structure even after 500 cycles, though showing fine expansion of primary particles. This result suggests that the conductive FTO interfacial layer dramatically prevents the Mn dissolution and volume expansion even during the ultrafast cycling process, which is also consistent with the EIS results (see Fig. S10) [39,51,52]. Therefore, in our study, strikingly improved ultrafast cycling performances of the FTO-LMO20 electrode have been achieved by introducing the novel conductive FTO interfacial layer on the LMO surface. The performance improvement can be attributed to the following three major effects of the conductive FTO interfacial layer (Fig. 9): (1) the optimized thickness helps to facilitate electron and Li⁺ diffusion at the LMO, improving the rate capability; (2) the conformal and dense thin-layer structure assists the prevention of the Mn dissolution and volume expansion during cycling, causing an enhancement of the cycling stability; and (3) the improved electrical conductivity accelerates the electron delivery at the entire electrode during the ultrafast cycling process, leading to striking ultrafast cycling performances with both a specific capacity and the capacity retention at 10 C.

4. Conclusions

In the present study, we successfully developed the conductive FTO interfacial layer on the LMO surface using the HUSPD. With optimization of the FTO deposition time, the LMO coated with the FTO deposited during 20 min (LMO-FTO20) represented a conformal and dense thin-layer structure on the LMO interfacial surface, which is effective to protect Mn dissolution and Jahn-Teller distortion of the LMO generated during cycling process. In addition, this structure showed improved effects of electrical conductivity and charge diffusion rate to improve electrochemical kinetics for the lithium storage performance. Therefore, when the electrode with LMO-FTO20 was used as a cathode material for the LIBs, the striking ultrafast lithium cycling performance (the specific capacity of 76.6 mAh g^{-1} with the capacity retention of 82.2% at 10 C after 500 cycles), together with an improved cycling capability (the specific capacity of 114.9 mAh g^{-1} and the capacity retention of 97.1% at 1 C after 100 cycles) was observed, which can be attributed to the following attractive functionalities of the conductive FTO interfacial layer. First, the impressive rate capability is caused by the efficient electron and Li⁺ diffusion resulting from the introduction of the conductive FTO interfacial layer with optimized thickness. Second, the improved cycling stability is ascribed to the effect of alleviated Mn dissolution and volume expansion by the conformal and dense thin-layer structure covered on the LMO surface. Third, the excellent lithium cycling performance is mainly related to the accelerated electron transport kinetics at the entire electrode by high electrical conductivity as the result of doping effect of F into SnO₂. Therefore, the optimum conductive FTO interfacial layer introduced on LMO surface is a promising strategy of cathode material for improving the ultrafast lithium storage performance in LIBs.

Acknowledgement

This work was supported by the Technology Innovation Program (10080656, Development of ceramic/carbon convergence and integration anode material for 10C fast charging Lithium ion battery) funded by the Ministry of Trade, Industry & Energy (MOTIE, Korea).

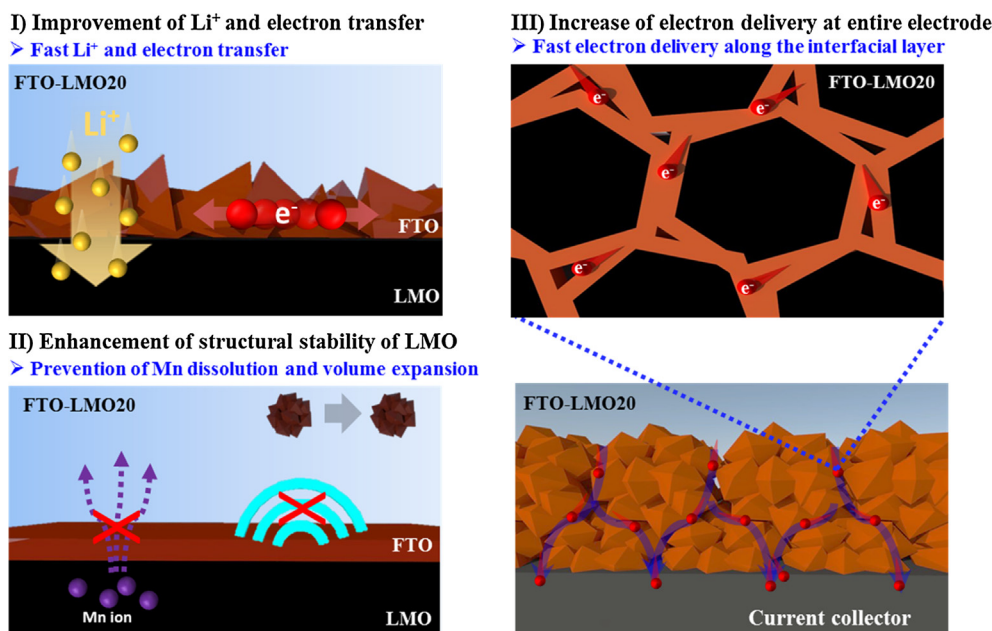


Fig. 9. Schematic illustration of the main effects on the FTO-LMO20 electrode for improving ultrafast lithium storage performances.

Appendix A. Supplementary material

Supplementary data to this article can be found online at <https://doi.org/10.1016/j.apsusc.2019.144057>.

References

- E. Senokos, Y. Ou, J.J. Torres, F. Sket, C. Gonazales, R. Marcilla, J.J. Vilatela, Energy storage in structural composites by introducing CNT fiber/polymer electrolyte interleaves, *Sci. Rep.* 8 (2018) 3407.
- D. Ren, X. Liu, X. Feng, L. Lu, M. Ouyang, J. Li, X. He, Model-based thermal runaway prediction of lithium-ion batteries from kinetics analysis of cell components, *Appl. Energy* 228 (2018) 633–644.
- Y. Zhang, L. Wang, Z. Guo, Y. Xu, Y. Wnag, H. Peng, High-performance lithium-air battery with a coaxial-fiber architecture, *Angew. Chem. Int. Ed.* 55 (2016) 4487–4491.
- K.C. Huang, H.H. Li, H.H. Fan, J.Z. Guo, Y.M. Xing, Y.P. Hu, X.L. Wu, J.P. Zhang, An in situ-fabricated composite polymer electrolyte containing large-anion lithium salt for all-solid-state LiFePO₄/Li batteries, *ChemElectroChem* 4 (2017) 2293–2299.
- J.M. Jeong, B.G. Choi, S.C. Lee, K.G. Lee, S.J. Chang, Y.K. Han, Y.B. Lee, H.U. Lee, S. Kwon, G. Lee, C.S. Lee, Y.S. Huh, Hierarchical hollow spheres of Fe₂O₃@polyaniline for lithium ion battery anodes, *Adv. Mater.* 25 (2013) 6250–6255.
- G.H. An, D.Y. Lee, H.J. Ahn, Tunneled mesoporous carbon nanofibers with embedded ZnO nanoparticles for ultrafast lithium storage, *ACS Appl. Mater. Interface* 9 (2017) 12478–12485.
- Z.Y. Jiang, Z.G. Qu, L. Zhou, W.Q. Tao, A microscopic investigation of ion and electron transport in lithium-ion battery porous electrodes using the lattice Boltzmann method, *Appl. Energy* 194 (2017) 530–539.
- G.H. An, H. Kim, H.J. Ahn, Improved ionic diffusion through the mesoporous carbon skin on silicon nanoparticles embedded in carbon for ultrafast lithium storage, *ACS Appl. Mater. Interface* 10 (2018) 6235–6244.
- H. Wang, Y. Yang, Y. Liang, J.T. Robinson, Y. Li, A. Jackson, Y. Cui, H. Dai, Graphene-wrapped sulfur particles as a rechargeable lithium-sulfur battery cathode material with high capacity and cycling stability, *Nano Lett.* 11 (2011) 2644–2647.
- Y.K. Sun, Z. Chen, H.J. Noh, D.J. Lee, H.G. Jung, Y. Ren, S. Wang, C.S. Yoon, S.T. Myung, K. Amine, Nanostructured high-energy cathode materials for advanced lithium batteries, *Nat. Mater.* 11 (2012) 942–947.
- D.Y. Shin, Y.G. Lee, H.J. Ahn, One-pot synthesis of aluminum oxide coating and aluminum doping on lithium manganese oxide nanoparticles for high performance energy storage system, *J. Alloy. Compd.* 727 (2017) 1165–1170.
- J.T. Son, H.G. Kim, Y.J. Park, New preparation method and electrochemical property of LiMn₂O₄ electrode, *Electrochim. Acta* 50 (2004) 453–459.
- K.M. Shaju, G.A. Bruce Peter, Stoichiometric nano-LiMn₂O₄ spinel electrode exhibiting high power and stable cycling, *Chem. Mater.* 20 (2008) 5557–5562.
- Y. Liu, X. Li, H. Guo, Z. Wang, Q. Hu, W. Peng, Y. Yang, Electrochemical performance and capacity fading reason of LiMn₂O₄/graphite batteries stored at room temperature, *J. Power Sources* 189 (2009) 721–725.
- Y. Kim, J. Lim, S. Kang, Investigation on the dissolution of Mn ions from LiMn₂O₄ cathode in the application of lithium ion batteries: first principle molecular orbital method, *Int. J. Quantum Chem.* 113 (2013) 148–154.
- J. Cho, T.J. Kim, Y.J. Kim, B. Park, Complete blocking of Mn³⁺ ion dissolution from a LiMn₂O₄ spinel intercalation compound by Co₃O₄ coating, *Chem. Commun.* 12 (2001) 1074–1075.
- X. Xie, D. Su, B. Sun, J. Zhang, C. Wang, G. Wang, Synthesis of single-crystalline spinel LiMn₂O₄ nanorods for lithium-ion batteries with high rate capability and long cycle life, *Chem. Eur. J.* 20 (2014) 17125–17131.
- D. Zhang, B.N. Popov, R.E. White, Electrochemical investigation of CrO_{2.65} doped LiMn₂O₄ as a cathode material for lithium-ion batteries, *J. Power Sources* 76 (1998) 81–90.
- S. Kuwabata, S. Masui, H. Yoneyama, Charge-discharge properties of composites of LiMn₂O₄ and polypyrrole as positive electrode materials for 4 V class of rechargeable Li batteries, *Electrochim. Acta* 44 (1999) 4593–4600.
- H.W. Ha, N.J. Yun, K. Kim, Improvement of electrochemical stability of LiMn₂O₄ by CeO₂ coating for lithium-ion batteries, *Electrochim. Acta* 52 (2007) 3236–3241.
- H. Liu, C. Cheng, K. Zhang Zongqiu, The effect of ZnO coating on LiMn₂O₄ cycle life in high temperature for lithium secondary batteries, *Mater. Chem. Phys.* 101 (2007) 276–279.
- Y. Shang, X. Lin, X. Lu, T. Huang, A. Yu, Nano-TiO₂(B) coated LiMn₂O₄ as cathode materials for lithium-ion batteries at elevated temperature, *Electrochim. Acta* 156 (2015) 121–126.
- B.R. Koo, D.H. Oh, D.H. Riu, H.J. Ahn, Improvement of transparent conducting performance on oxygen-activated fluorine-doped tin oxide electrodes formed by horizontal ultrasonic spray pyrolysis deposition, *ACS Appl. Mater. Interfaces* 9 (2017) 44584–44592.
- B.R. Koo, D.H. Oh, H.J. Ahn, Influence of Nb-doped TiO₂ blocking layers as a cascading band structure for enhanced photovoltaic properties, *Appl. Surf. Sci.* 433 (2018) 27–34.
- A. Kolmakov, Y. Zhang, G. Cheng, M. Moskovits, Detection of CO and O₂ using tin oxide nanowire sensors, *Adv. Mater.* 15 (2003) 997.
- B.R. Koo, J.W. Bae, H.J. Ahn, Low-temperature conducting performance of transparent indium tin oxide/antimony tin oxide electrodes, *Ceram. Int.* 43 (2017) 6124–6129.
- X. Meng, L. Li, J. Liu, X. Han, W. Zhang, X. Liu, Q. Xu, Surface modification of Li-rich layered Li[Li_{0.17}Ni_{0.17}Co_{0.10}Mn_{0.56}]O₂ oxide with LiV₃O₉ as a cathode material for Li-ion batteries, *J. Alloy. Compd.* 690 (2017) 256–266.
- B.R. Koo, H.J. Ahn, Fast-switching electrochromic properties of mesoporous WO₃ films with oxygen vacancy defects, *Nanoscale* 9 (2017) 17788.
- G.H. An, J.I. Sohn, H.J. Ahn, Hierarchical architecture of hybrid carbon-encapsulated hollow manganese oxide nanotubes with a porous-wall structure for high-performance electrochemical energy storage, *J. Mater. Chem. A* 4 (2016) 2049.
- S.C. Han, S.P. Singh, Y.H. Hwang, E.G. Bae, B.K. Park, K.S. Sohn, M. Pyo, Gadolinium-doped LiMn₂O₄ cathode in Li ion batteries: understanding the stabilized structure and enhanced electrochemical kinetics, *J. Electrochem. Soc.* 159 (2012) A1867–A1873.
- V. Senthilkumar, P. Vickraman, R. Racikumar, Synthesis of fluorine doped tin oxide nanoparticles by sol-gel technique and their characterization, *J. Sol-Gel Sci. Technol.* 53 (2010) 316–321.
- X. Yi, X. Wang, B. Ju, H. Shu, W. Wen, R. Yu, D. Wang, X. Yang, Effective enhancement of electrochemical performance for spherical spinel LiMn₂O₄ via Li ion conductive Li₂ZrO₂ coating, *Electrochim. Acta* 134 (2014) 143–149.
- S. Sim, P. Oh, S. Park, J. Cho, Critical thickness of SiO₂ coating layer on core@shell bulk@nanowire Si anode materials for Li-ion batteries, *Adv. Mater.* 25 (2013) 4498–4503.

- [34] Y. Fu, Y. Li, X. Zhang, Y. Liu, J. Qiao, J. Zhang, D.P. Wilkinson, Novel hierarchical SnO₂ microsphere catalyst coated on gas diffusion electrode for enhancing energy efficiency of CO₂ reduction to formate fuel, *Appl. Energy* 175 (2016) 536–544.
- [35] Q. Kuang, S.F. Li, Z.X. Xie, S.C. Lin, X.H. Zhang, S.Y. Xie, R.B. Huang, L.S. Zheng, Controllable fabrication of SnO₂-coated multiwalled carbon nanotubes by chemical vapor deposition, *Carbon* 44 (2006) 1166–1172.
- [36] G.H. An, D.Y. Lee, Y.J. Lee, H.J. Ahn, Ultrafast lithium storage using antimony-doped tin oxide nanoparticles sandwiched between carbon nanofibers and a carbon skin, *ACS Appl. Mater. Interfaces* 8 (2016) 30264–30270.
- [37] G.H. An, D.Y. Lee, H.J. Ahn, Vanadium nitride encapsulated carbon fibre networks with furrowed porous surfaces for ultrafast asymmetric supercapacitors with robust cycle life, *J. Mater. Chem. A* 5 (2017) 19714.
- [38] D.Y. Sin, B.R. Koo, H.J. Ahn, Hollow lithium manganese oxide nanotubes using MnO₂-carbon nanofiber composites as cathode materials for hybrid capacitors, *J. Alloy. Compd.* 696 (2017) 290–294.
- [39] Y.W. Lee, D.M. Kim, S.J. Kim, M.C. Kim, H.S. Choe, K.H. Lee, J.I. Sohn, S.N. Cha, J.M. Kim, K.W. Park, In situ synthesis and characterization of ge embedded electrospun carbon nanostructures as high performance anode material for lithium-ion batteries, *ACS Appl. Mater. Interfaces* 8 (2016) 7022–7029.
- [40] Y.M. Lin, H.C. Wu, Y.C. Yen, Z.Z. Guo, M.H. Yang, H.M. Chen, H.S. Sheu, N.L. Wu, Enhanced high-rate cycling stability of LiMn₂O₄ cathode by ZrO₂ coating for Li-ion battery, *J. Electrochem. Soc.* 152 (2005) A1526–A1532.
- [41] S. Zhao, Y. Bai, L. Ding, B. Wang, W. Zhang, Enhanced cycling stability and thermal stability of YPO₄-coated LiMn₂O₄ cathode materials for lithium ion batteries, *Solid State Ion.* 247 (2013) 22–29.
- [42] S. Zhao, Q. Chang, K. Jiang, Y. Bai, Y. Yang, W. Zhang, Performance improvement of spinel LiMn₂O₄ cathode material by LaF₃ surface modification, *Solid State Ion.* 253 (2013) 1–7.
- [43] S. Zhao, Y. Bai, Q. Chang, Y. Yang, W. Zhang, Surface modification of spinel LiMn₂O₄ with FeF₃ for lithium ion batteries, *Electrochem. Acta* 108 (2013) 727–735.
- [44] J. Cao, G. Cao, H. Yu, J. Xie, X. Zhao, Synthesis and electrochemical performance of YF₃-coated LiMn₂O₄ cathode materials for Li-ion batteries, *Rare Metals* 30 (2011) 39.
- [45] J. Zeng, M. Li, X. Li, C. Chen, D. Xiong, L. Dong, D. Li, A. Lushington, X. Sun, A novel coating onto LiMn₂O₄ cathode with increased lithium ion battery performance, *Appl. Surf. Sci.* 317 (2014) 884–891.
- [46] A. Tron, Y.D. Park, J. Mun, AlF₃-coated LiMn₂O₄ as cathode material for aqueous rechargeable lithium battery with improved cycling stability, *J. Power Sources* 325 (2016) 360–364.
- [47] X. Zhang, Y. Xu, H. Zhang, C. Zhao, X. Qian, Structure and cycle stability of SrHPO₄ coated LiMn₂O₄ cathode materials for lithium-ion batteries, *Electrochem. Acta* 145 (2014) 201–208.
- [48] C. Wei, H. Fei, Y. An, Y. Zhang, J. Feng, *Electrochem. Acta* 309 (2019) 362–370.
- [49] A.M. Hashem, A.E. Abdel-Ghany, H.M. Abuzeid, R.S. El-Tawil, S. Indris, H. Ehrenberg, A. Mauger, C.M. Julien, EDTA as chelating agent for sol-gel synthesis of spinel LiMn₂O₄ cathode material for lithium batteries, *J. Alloy. Compd.* 737 (2018) 758–766.
- [50] A. Rougier, K.A. Striebel, S.J. Wen, E.J. Cairns, Cyclic voltammetry of pulsed laser deposited Li_xMn₂O₄ thin films, *J. Electrochem. Soc.* 145 (1998) 2975.
- [51] K.Y. Chung, C.W. Ryu, K.B. Kim, Onset mechanism of Jahn-Teller distortion in 4 V LiMn₂O₄ and its suppression by LiM_{0.05}Mn_{1.95}O₄ (M = Co, Ni) coating, *J. Electrochem. Soc.* 152 (2005) A791–A795.
- [52] N. Ohta, K. Takada, L. Zhang, R. Ma, M. Osada, T. Sasaki, Enhancement of the high-rate capability of solid-state lithium batteries by nanoscale interfacial modification, *Adv. Mater.* 18 (2006) 2226–2229.